

# In-situ synthesis of carbon nanotubes on 3D printed carbon fiber reinforced polymer



Changchun Wang<sup>a</sup>, Lijun Li<sup>a,\*</sup>, Liang He<sup>a</sup>, Chao Wang<sup>b</sup>, Kailiang Ess<sup>c</sup>, Lili Gu<sup>d</sup>, Tianshu Peng<sup>e</sup>

<sup>a</sup> Gemmological Institute, China University of Geosciences, Wuhan 430074, PR China  
<sup>b</sup> Hubei Gem and Jewelry Engineering Technology Research Center, Wuhan 430074, PR China  
<sup>c</sup> School of Materials Science and Engineering, Huazhong University of Science and Technology, Wuhan 430074, PR China  
<sup>d</sup> Mechanical Engineering, University of Birmingham, Birmingham B15 2TT, UK  
<sup>e</sup> School of Electrical and Electronic Engineering, Huazhong University of Science and Technology, Wuhan 430074, PR China  
 WMG, Materials Engineering Centre, University of Warwick, CV4 7AL Coventry, UK

## ARTICLE INFO

### Keywords:

Carbon nanotubes  
 3D printing  
 In-situ synthesis  
 Carbon fiber reinforced polymer  
 Mechanical properties

## ABSTRACT

Carbon nanotubes (CNTs) were synthesized in-situ on 3D printed carbon fiber reinforced polymer (CFRP) using a chemical vapor deposition (CVD) process. The synthesis was carried out at 900 °C for 2 h. The CNTs were synthesized on the surface of the CFRP, and the length of the CNTs was in the range of 1–5 μm. The CNTs were randomly distributed on the surface of the CFRP. The tensile strength of the CFRP with CNTs was 47.8 MPa, which was 2.7 times higher than that of the CFRP without CNTs (17.7 MPa). The elongation at break of the CFRP with CNTs was 32.3%, which was 2–18% higher than that of the CFRP without CNTs. The results show that the in-situ synthesis of CNTs on CFRP can significantly improve the mechanical properties of CFRP.

## 1. Introduction

Carbon nanotubes (CNTs) are a new type of carbon material with excellent mechanical, electrical, and thermal properties. They have been widely used in various fields, such as aerospace, automotive, and sports equipment. However, the high cost and low production efficiency of CNTs have limited their large-scale application. In-situ synthesis of CNTs on the surface of carbon fiber reinforced polymer (CFRP) is a promising method to improve the mechanical properties of CFRP. In this study, CNTs were synthesized in-situ on CFRP using a chemical vapor deposition (CVD) process. The synthesis was carried out at 900 °C for 2 h. The CNTs were synthesized on the surface of the CFRP, and the length of the CNTs was in the range of 1–5 μm. The CNTs were randomly distributed on the surface of the CFRP. The tensile strength of the CFRP with CNTs was 47.8 MPa, which was 2.7 times higher than that of the CFRP without CNTs (17.7 MPa). The elongation at break of the CFRP with CNTs was 32.3%, which was 2–18% higher than that of the CFRP without CNTs. The results show that the in-situ synthesis of CNTs on CFRP can significantly improve the mechanical properties of CFRP.

(2DG), CNTs were synthesized in-situ on CFRP using a CVD process. The synthesis was carried out at 900 °C for 2 h. The CNTs were synthesized on the surface of the CFRP, and the length of the CNTs was in the range of 1–5 μm. The CNTs were randomly distributed on the surface of the CFRP. The tensile strength of the CFRP with CNTs was 47.8 MPa, which was 2.7 times higher than that of the CFRP without CNTs (17.7 MPa). The elongation at break of the CFRP with CNTs was 32.3%, which was 2–18% higher than that of the CFRP without CNTs. The results show that the in-situ synthesis of CNTs on CFRP can significantly improve the mechanical properties of CFRP.

\* Corresponding author. E-mail address: [llj@cg.cug.edu.cn](mailto:llj@cg.cug.edu.cn) (L. Li).



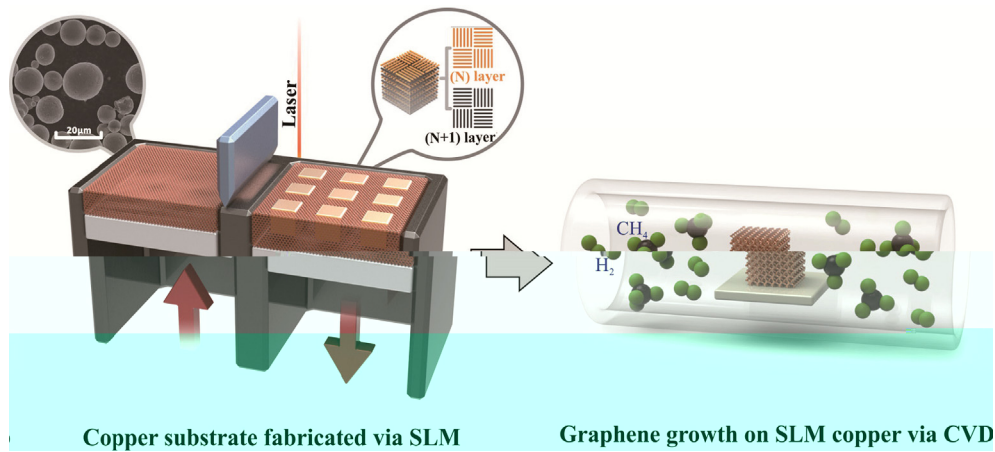


Fig. 1. Schematic diagram of the SLM process for copper substrate fabrication and subsequent CVD graphene growth on SLM copper via CVD.

ASTM B193-2002  
 (5 10 10<sup>3</sup>)  
 LFA457, G  
 (SENTERRA, B  
 3DG/C  
 514  
 (VNA, A  
 KPNA-N5244A,  
 2-18 GH  
 SE  
 SE  
 E . 2-5

SLM  
 in-situ  
 CVD  
 (F  
 (A), 26.7%  
 (B), 16.7%  
 (C), 26.7%  
 (D).  
 LED (J/ ) 27  
 (E . 6,  
 (SI).  
 T  
 (D), w  
 130 μ  
 (D), w  
 28 .

3. Results and discussion

3.1. Formation of SLM copper

3.1.1. SLM manufacturing of copper under different line energy densities

T  
 w  
 D ff

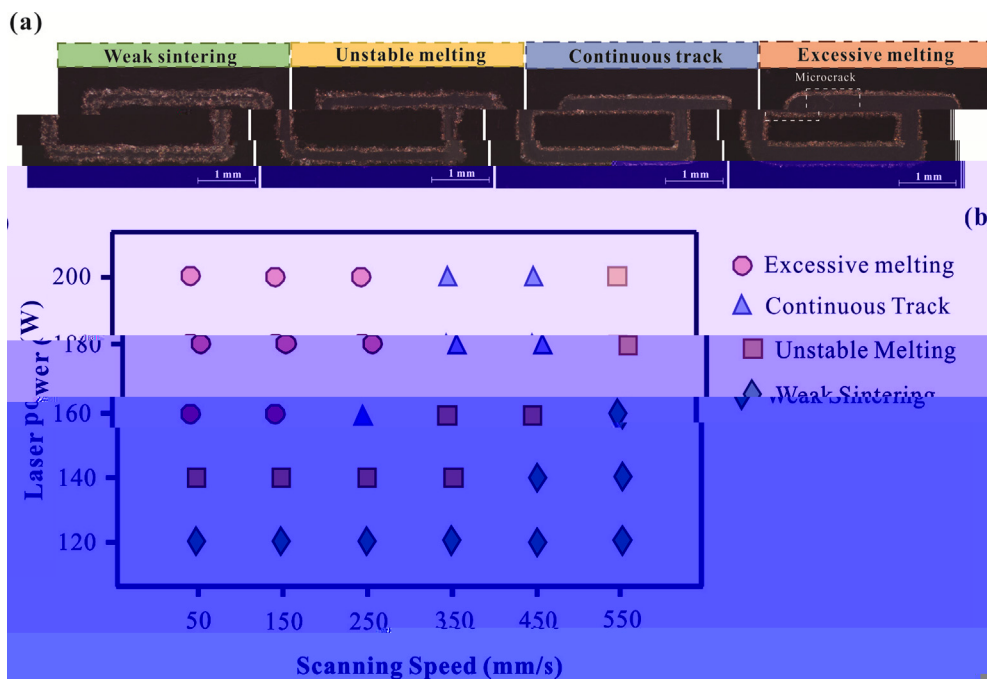


Fig. 2. (a) SEM images of SLM copper tracks under different conditions. (b) Scatter plot of Laser Power vs Scanning Speed showing the regions for different conditions.

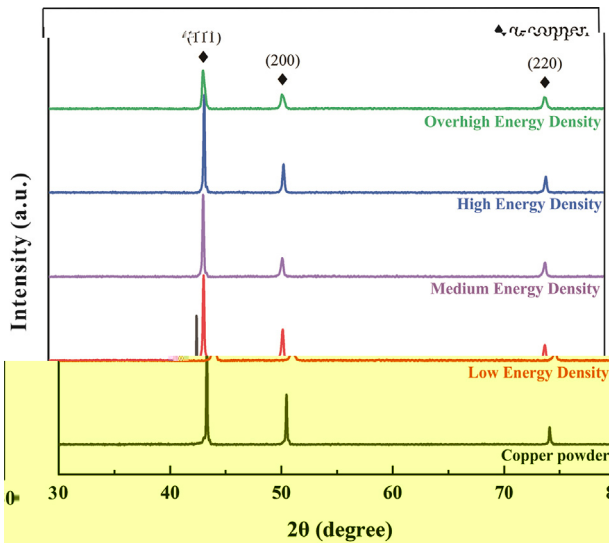


Fig. 3. XRD patterns of copper powder at different energy densities. (a) 3000 J/cm<sup>3</sup>, (b) 857 J/cm<sup>3</sup>, (c) 128 J/cm<sup>3</sup>, (d) 285 J/cm<sup>3</sup>.

3.1.2. Formation of anisotropic microstructure under different volumetric energy density

The XRD patterns of copper powder at different energy densities are shown in Fig. 3. The main peaks are indexed to the copper powder (JCPDS No. 03-065-0897). The peak positions are 44.5° (111), 50.4° (200) and 73.5° (220). The peak intensity of the (111) plane is significantly higher than that of the (200) and (220) planes, indicating a strong preferred orientation of the copper powder along the (111) plane. The preferred orientation of the copper powder is further confirmed by the pole figure (PF) plot in Fig. 4a, which shows a high intensity of the (111) plane along the z-axis. The preferred orientation of the copper powder is caused by the high energy density of the laser, which leads to the preferential growth of the (111) plane.

The XRD patterns of copper powder at different energy densities are shown in Fig. 3. The main peaks are indexed to the copper powder (JCPDS No. 03-065-0897). The peak positions are 44.5° (111), 50.4° (200) and 73.5° (220). The peak intensity of the (111) plane is significantly higher than that of the (200) and (220) planes, indicating a strong preferred orientation of the copper powder along the (111) plane. The preferred orientation of the copper powder is further confirmed by the pole figure (PF) plot in Fig. 4a, which shows a high intensity of the (111) plane along the z-axis. The preferred orientation of the copper powder is caused by the high energy density of the laser, which leads to the preferential growth of the (111) plane.

The XRD patterns of copper powder at different energy densities are shown in Fig. 3. The main peaks are indexed to the copper powder (JCPDS No. 03-065-0897). The peak positions are 44.5° (111), 50.4° (200) and 73.5° (220). The peak intensity of the (111) plane is significantly higher than that of the (200) and (220) planes, indicating a strong preferred orientation of the copper powder along the (111) plane. The preferred orientation of the copper powder is further confirmed by the pole figure (PF) plot in Fig. 4a, which shows a high intensity of the (111) plane along the z-axis. The preferred orientation of the copper powder is caused by the high energy density of the laser, which leads to the preferential growth of the (111) plane.

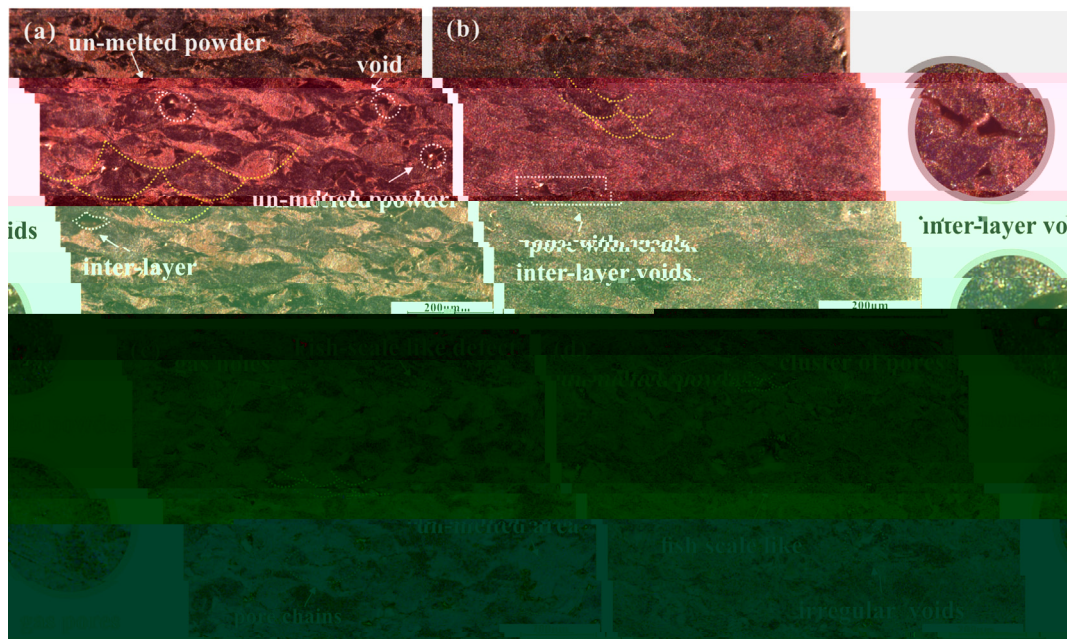


Fig. 4. SEM micrographs of copper powder at different energy densities: (a) 3000 J/cm<sup>3</sup>, (b) 857 J/cm<sup>3</sup>, (c) 128 J/cm<sup>3</sup>, (d) 285 J/cm<sup>3</sup>.

. K . K K K s w . K

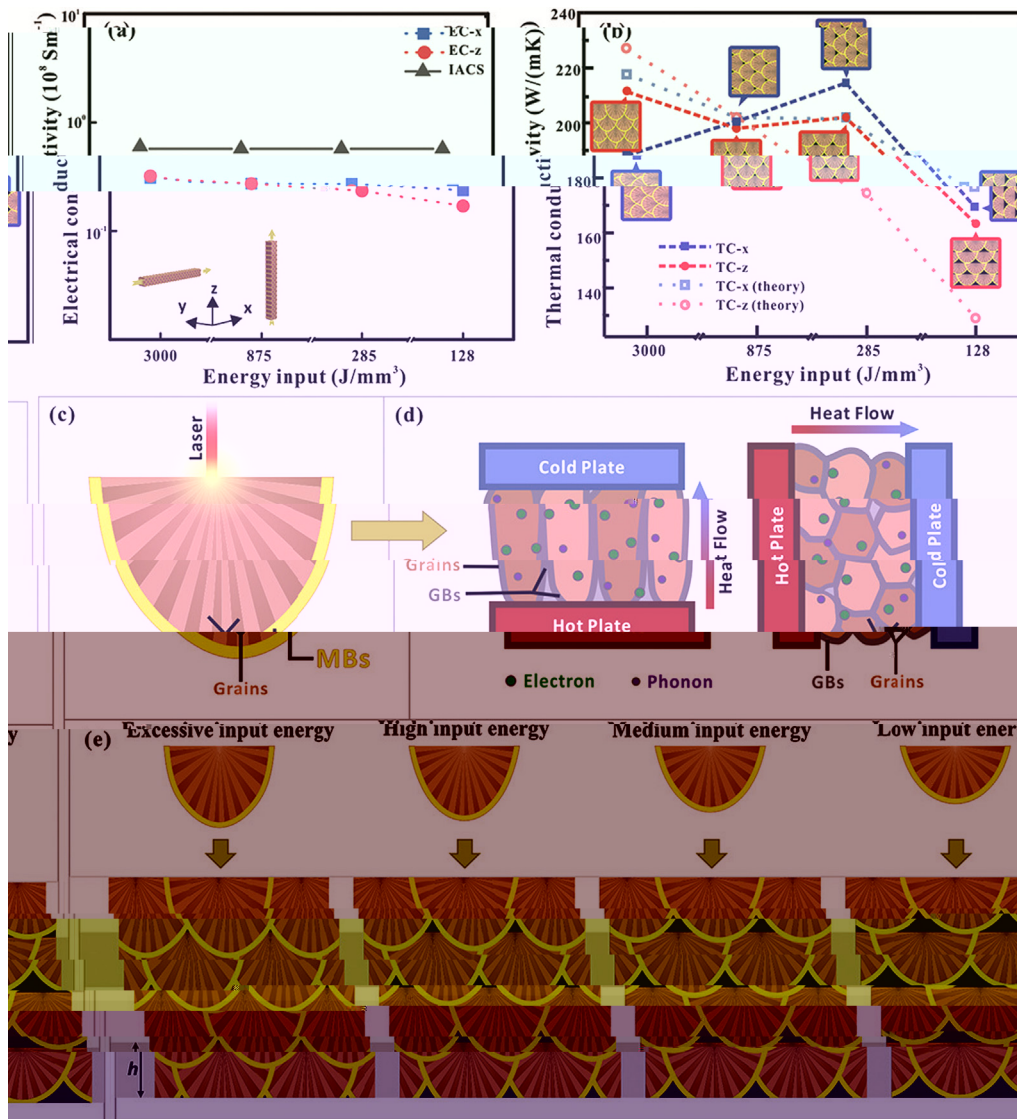


Fig. 7. (a) Electrical conductivity of TC-x, EC-z, and IACS as a function of energy input. (b) Thermal conductivity of TC-x and TC-z as a function of energy input. (c) Schematic of laser irradiation on a material surface. (d) Schematic of heat flow through a material between hot and cold plates, showing electron and phonon transport. (e) Schematic showing the effect of excessive, high, medium, and low input energy on the material's microstructure.

3.3. Morphology and structure of CVD 3DG/Cu porous scaffolds

The morphology and structure of CVD 3DG/Cu porous scaffolds were investigated by SEM, TEM, and EDS. The scaffolds were prepared by CVD of Cu on 3DG. The scaffolds exhibited a porous structure with interconnected walls and large pores. The walls were composed of Cu nanowires and nanorods. The scaffolds were characterized by a high surface area and a porous structure. The scaffolds were prepared by CVD of Cu on 3DG. The scaffolds exhibited a porous structure with interconnected walls and large pores. The walls were composed of Cu nanowires and nanorods. The scaffolds were characterized by a high surface area and a porous structure.

The scaffolds were prepared by CVD of Cu on 3DG. The scaffolds exhibited a porous structure with interconnected walls and large pores. The walls were composed of Cu nanowires and nanorods. The scaffolds were characterized by a high surface area and a porous structure. The scaffolds were prepared by CVD of Cu on 3DG. The scaffolds exhibited a porous structure with interconnected walls and large pores. The walls were composed of Cu nanowires and nanorods. The scaffolds were characterized by a high surface area and a porous structure.



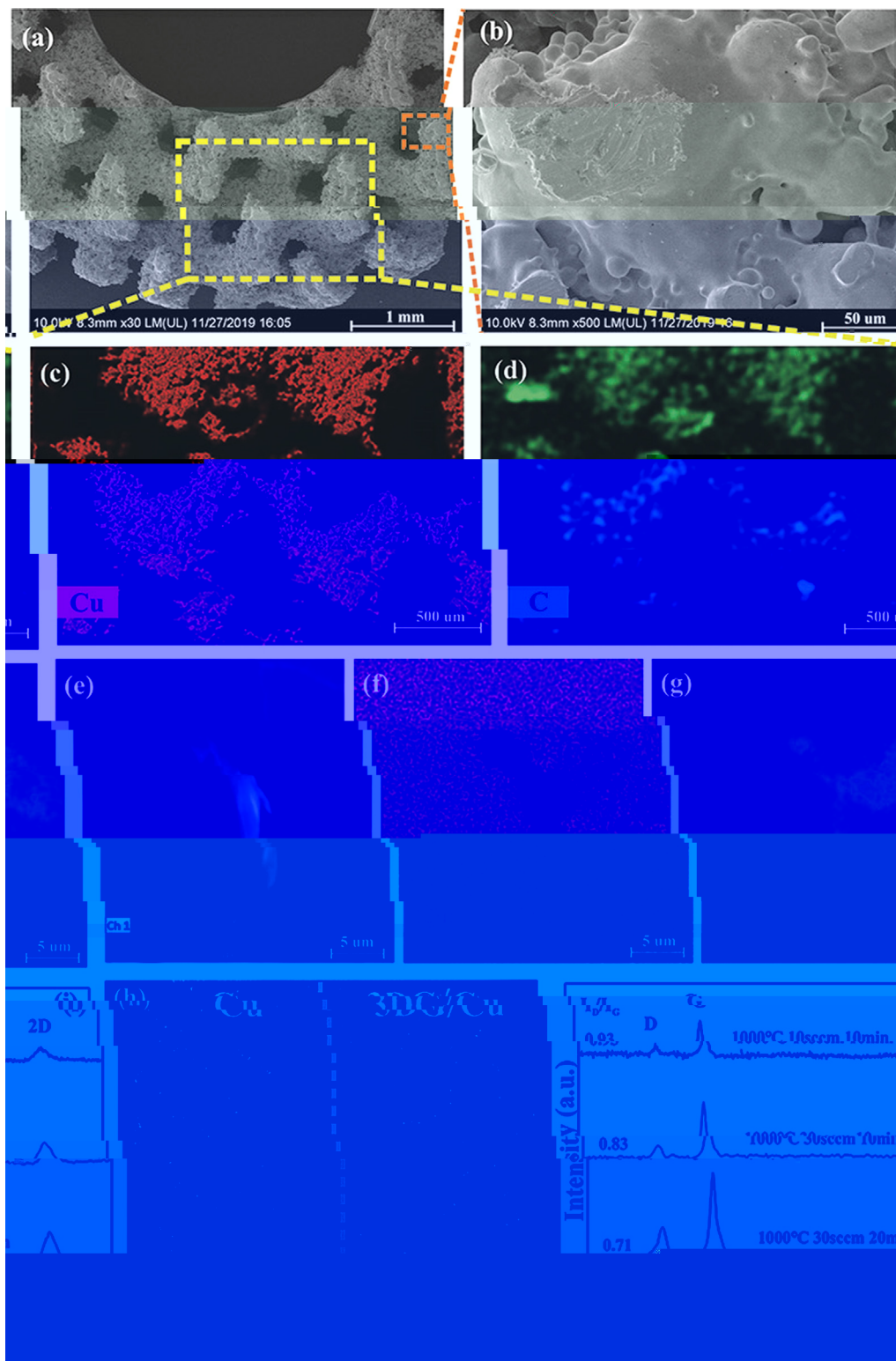


Fig. 8. (a) SEM image of 3DG/C porous scaffold; (b) SEM image of 3DG/C porous scaffold; (c) EDS map of Cu; (d) EDS map of C; (e) EDS line scan of Cu; (f) EDS line scan of C; (g) Raman spectra of 3DG/C porous scaffolds at different temperatures.

The  $I_D/I_G$  ratio of the Raman spectra of 3DG/C porous scaffolds at different temperatures is shown in Table 1. The  $I_D/I_G$  ratio of the Raman spectra of 3DG/C porous scaffolds at 1000 °C is 0.71, which is lower than that of 3DG/C porous scaffolds at 1000 °C (0.83) and 1000 °C (0.93). This indicates that the 3DG/C porous scaffolds at 1000 °C have a higher degree of graphitization than those at 1000 °C (0.83) and 1000 °C (0.93).

### 3.4. Thermal property and EMI shielding effectiveness of 3DG/Cu porous scaffolds

The thermal stability of 3DG/Cu porous scaffolds was evaluated by TGA. The TGA curves of 3DG/Cu porous scaffolds at different temperatures are shown in Fig. 9. The weight loss of 3DG/Cu porous scaffolds at 1000 °C is 26.8%, which is higher than that of 3DG/C porous scaffolds (14.8%).

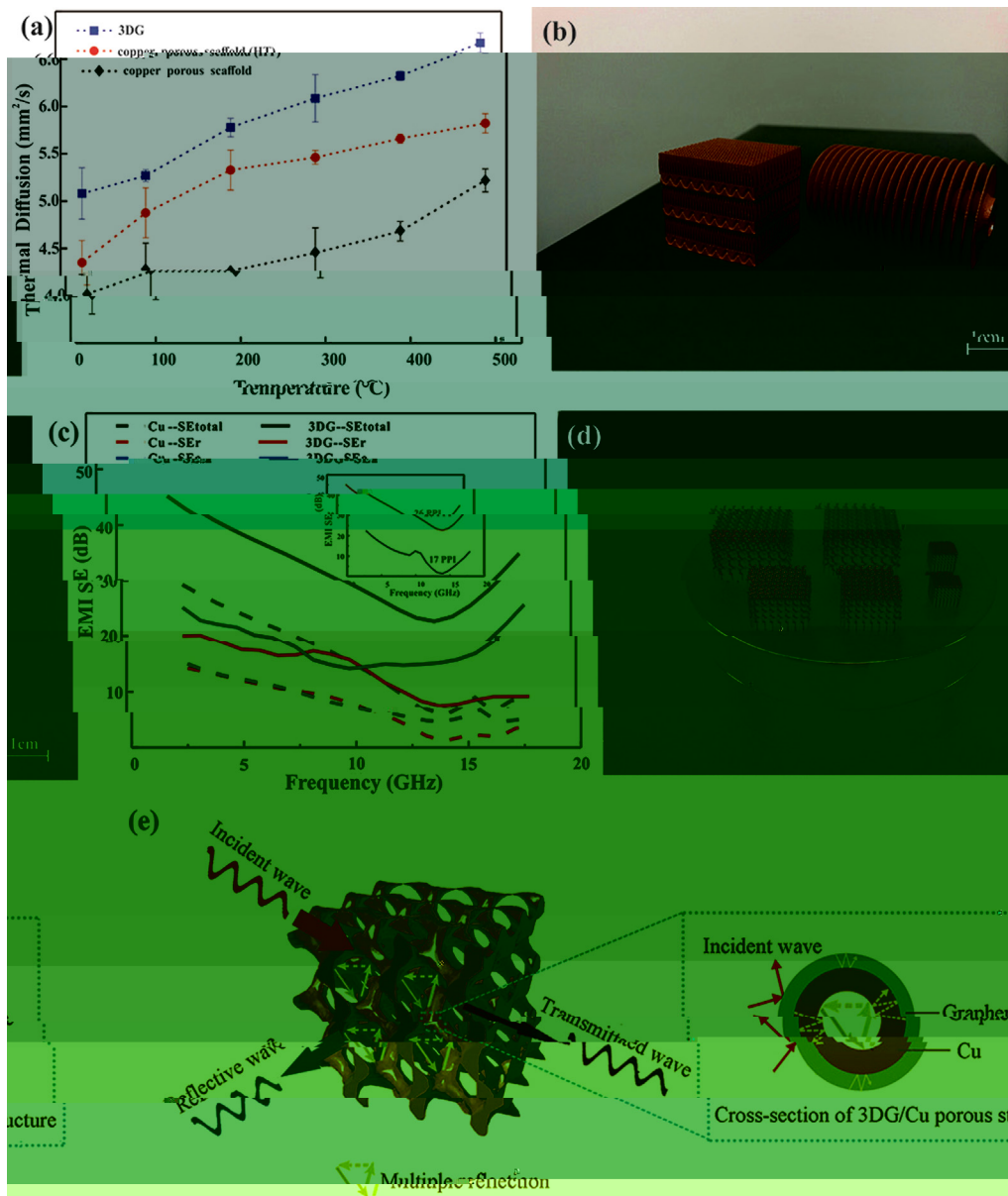


Fig. 9. (a) Thermal Diffusion (mm<sup>2</sup>/s) vs Temperature (°C) for 3DG, copper porous scaffold (17P), and copper porous scaffold. (b) 3D schematic of 3DG/Cu porous structure. (c) EMI SE (dB) vs Frequency (GHz) for Cu-SEtotal, 3DG-SEtotal, Cu-SEr, and 3DG-SEr. (d) SEM image of the porous structure. (e) Schematic of wave interaction with the porous structure showing incident, reflective, and transmitted waves, and a cross-section of the 3DG/Cu porous structure.

Table 1

Coating materials	Substrate	Method	Maximum shielding efficiency (dB)	Improvement of thermal property (%)	Ref
G	G	I	37	-	50
G	PS	H	29.3	-	56
G	PMMA	S	19	-	57
C /G	/C	S	-	8.5	58
G	N	F	-	554	59
G	C-N	E	20	-	60
G	C	P	-	2.4	61
G	s C	F	47	6.3	62
G	C	CVD + SLM	47.8	27	T s w

Note: ( ) -PPMA, ( ) -PS.



HT s s K s K K s K  
*in-situ* wK (F .9a). S K s - K -K sK -  
 K K K 3DG/C s s ff ss ss s -  
 K . IK s s w K K K K HT s s  
 K s K K s wK s , K sK K K 3DG/C s Ks -  
 1-2 s K K K K I K s s , s s  
 s s s K w sK K K  
 K w K , K s K K K s . W K  
 s K K K K s sK K SLM  
 - ssfl w K (w K fl  
 K ss K 500 μ ) . K-K sK K w s s ss  
 K (F .9b), K sK K K K K K  
 K s w K K s K K K  
 sK K -s . G K K K s s K K K -  
 s s K s, K sK K s , K K ss,  
 w K s K K s K K K K -  
 K K K K K K K s sK K  
 (T 1). IK K K K s w s K  
 s K w K s s s. OK K -  
 K s K K K w K K K  
 s , N  
 T sK K K K K K 3DG/C s s ff  
 EMI, K EMI SE, w K s K K K K K  
 K K (EM) K , w s sK K K  
 2-18 GH (F .9c), K s K  
 K W K *in-situ* w  
 s s ff , K SE s 15.9 K 32.3 B, w K  
 47.8 B (88.2% s ), s ss K  
 K K 20 B. T K  
 K K s 3DG/C fi K K  
 K s sK K. J K K . 44 K KEMI K  
 s Ks s w K s s K. T EMI SE  
 K K 133% K w K s s K  
 s K ( . , s K s ) 20 K 110 PPI ( s ).  
 R Ks 45 s w K K s K s  
 K K s K K K K EMI  
 . W s s K s s K s K  
 17 K 26 PPI (F .9c insert). K 105% K  
 EMI SE. I K w s, K EMI s K s sK  
 s ff s K w K K K K s SLM. T  
 3DG/C s sK K 26 PPI K EMI SE  
 32.3 B, s K 99.9% K EMI w s. T s  
 s w s s 60 K  
 (30 K s K K K s ff ) 46 . T EMI  
 s s s 3DG/C w K s - s K -  
 s s sK T s 1. IK K K EMI SE  
 K 3DG/C w s K K s  
 K 3D - s s Ks, K s  
 K K K .  
 T s s EMI s sK fl K (SE<sub>r</sub>), s K  
 (SE<sub>a</sub>) K fl K s K K (EM) w s 47 ,  
 w K w K s, K  
 K s, K s s K s, s K  
 48 . R s s 49 K K K w K  
 K K, s, fl K K K  
 w s, w s K K K K K w K K s s.  
 T s K K s w s K KEM w  
 ss s K K K K K K K fi  
 K s 50 . R K s s EMI K  
 s . T sK s K s K K -  
 s K K w K w K K K  
 w K K fi s, s s C 51 . F K  
 K s K - Ks  
 K K 52 S O<sub>2</sub> 53 . W K K K s  
 3DG/C s s ff s w K K

s sK s s s w K s fi K s K  
 SE<sub>r</sub>, SE<sub>a</sub>, s s K s w F .9e. W K w s  
 w w K K s K 3DG/C s s ff , s  
 w s w K fl K K K K w K -  
 w s K K s K s s ff . S K -  
 s , K sK K K 3DG/C s Ks -  
 s K s fl K s s K s  
 w s w K K s K K w s. T  
 EM w s fi sK K K w K K  
 sK K K K K w K K EMI s, s K  
 K , K K K ss K K SE<sub>r</sub>. O K  
 K , K K K s K  
 K s ff , w w s K fi K K EM  
 w s K K K s ff , s s K K EM -  
 s ss K s s s s. T  
 K K s K ff s w K K  
 w fi K J K 54 . IK s w K K K K  
 K fi K s K w s K K K  
 K K K fl K ff K. M , K  
 s s K K K K  
 K s sK K, K s s  
 w K s s, K K K fl K s s K  
 EM w s s K K , K s K K K ss K  
 EM w s. T s K K K w s  
 w K K s 44 . T s s ss s K  
 K s w K K 3D K s K  
 K K K s K K K sKEM w s w s  
 K K s. I K sK , K sK CVD K s  
 R s K s K K K s  
 sK Ks s S K 3.3 s K s s K K s  
 K K K K ss s s K K ,  
 K s 55 . IK s  
 K K EM w s w K K K K s, w K s  
 s K K s K K K K ss. O K w , K  
 s sK K K 3DG/C s Ks K K K  
 fl K , s K , s K K fi  
 s K . T K ss K s s K K  
 s K w s K s ff s  
 K s K K K

4. Conclusions

A K 3DG/C s s ff w s s ss K w K  
 s *in-situ* s K CVD K  
 T s K sK K K s s K w  
 K K s s ff K . W K K K  
 s K K sK K K , K 3DG/C  
 sK K s K K EMI SE  
 15.9 ( s ) K 32.3 B, K  
 47.8 B (88.2% s ), s w s 26.8% s K K  
 ff s . T 3DG/C sK K K s K  
 ff K fl K , s K K fl K s -  
 s s. T s K EMI K K K  
 K K3DG/C s s ff s s K K  
 K s EMI s K K

Credit authorship contribution statement

Kaka Cheng: C K K , M K , F s s,  
 W K - K Wei Xiong: V K , I sK K , W K -  
 K Yan Li: W K - w & K , F s K ,  
 R s s, S s . Liang Hao: F s K . Chunze Yan:  
 R s s, F s K . Zhaoqing Li: V K . Zhufeng Liu:  
 F s s. Yushen Wang: I sK K , S K . Khamis Essa:  
 W K - w & K . Li Lee: D K . Xin Gong: S K  
 Ton Peijs: W K - w & K , S s .



M 2019;34(5):489–98.

53 W B, C M, L M. R s: Kw K - ffi  
K K s K K K s. A M K  
2014;26:3484–9.

54 C H, W S, J , J, , C J, K . S K ff K F<sub>3</sub>O<sub>4</sub>  
K s fl ( fl ) s fi s w K  
K ss K K K s . C s P KA  
2019;121:139–48.

55 W L, J, Q. T ff K MWCNTs K w K -  
K s K-MWCNTs s Ks. J M K S : M K E K  
2015;26(3):1895–9.

56 D , P GR, H P, Q F, M B , ML. Effi K K K  
K s Kw K / s K s K. J. M K  
C 2012;22:18772–4.

57 HB, Q, WG, H , T -  
s K K s . ACS A M K I K s  
2011;3:918–24.

58 S A, U N, T V. T K  
- s s K K s K  
M KR 2016. <https://doi.org/10.1051/w/2016021>.

59 P MT, J H, R ff RS, S L. T K s K K - s  
K K s w- K K K. N L K  
2012;12:2959–64.

60 J K, H, H , D . P C -N  
K K w K s, s s K K K K M K L  
2017;122:244–7.

61 R H, L S, B S, K TW, L DS, L HJ, K . T - s s  
K s K K s w K K K ss K -  
S R 2015. <https://doi.org/10.1038/s12710-015-0127-1>.

62 T, F SG, L , G Q, L G, R KP, K . S s  
K K K s K K K K  
s Ks s K K 3D w s/K  
w . M K S E A-SK 2020. <https://doi.org/10.1016/j.compositesa.2019.105670>.

63 R DA, M LE, M K E, H DH, M K JL, M BI, K .  
N K K- s K K K K K s  
K K K s K K . A K  
M 2011;59(10):4088–99.

64 EK s SF, L KC, S s VK, M IC. T K KsK . J T sK  
E . 1973;1(1):10–38.